Cost-Effective Soil Carbon Sensing with Wi-Fi and Optical Signals

Jian Ding
Yale University

Ranveer Chandra
Microsoft

Rattan Lal
Ohio State University

Leandros Tassiulas
Yale University

Abstract

Soil carbon is a critical factor in maintaining soil health and combating climate change. Understanding and managing soil carbon levels is essential for sustainable agriculture and environmental protection. However, current methods for measuring soil carbon are time-consuming and costly, hindering efforts to monitor soil health and increase carbon sequestration. In this paper, we propose Scarf, a novel soil carbon sensing approach that combines widely accessible radio frequency (RF) and optical signals to detect soil carbon contents without dedicated hardware. Our key insight is that soil carbon content closely correlates with two indicators: the effective permittivity derived from RF signals and soil lightness determined from soil surface images. We mathematically model the correlations and leverage the non-linear correlation between the two signal modalities to compute soil carbon content. We employ machine learning to model relationships that cannot be captured by traditional mathematical equations. Our experimental results indicate that Scarf can achieve high soil carbon prediction accuracy that is comparable to the state-of-the-art soil carbon sensing techniques which cost US$1000s.

CCS Concepts

• Human-centered computing → Ubiquitous and mobile computing; **• Computer systems organization → Embedded and cyber-physical systems**.

Keywords

Soil carbon, Sustainable agriculture, Wi-Fi, Smartphone image, Machine Learning, Multi-modality

ACM MobiCom '24, November 18–22, 2024, Washington D.C., DC, USA

ACM ISBN 979-8-4007-0489-5/24/11
https://doi.org/10.1145/3636534.3690675

ACM Reference Format:
Jian Ding, Ranveer Chandra, Rattan Lal, and Leandros Tassiulas. 2024. Cost-Effective Soil Carbon Sensing with Wi-Fi and Optical Signals. In *The 30th Annual International Conference on Mobile Computing and Networking (ACM MobiCom '24), November 18–22, 2024, Washington D.C., DC, USA.* ACM, New York, NY, USA, 15 pages. https://doi.org/10.1145/3636534.3690675

1 Introduction

Over the past few decades, soil carbon has emerged as a critical focus for researchers and farmers, driven by its pivotal role in climate change, soil health, and agricultural sustainability. As part of the global carbon cycle (GCC), soil carbon helps remove carbon dioxide (CO_2) from the atmosphere through a process known as carbon sequestration. During this process, CO_2 is first absorbed by plants through photosynthesis, followed by the transfer of a portion of the carbon into soil through the decomposition of plant material. Soil carbon is also crucial in fostering soil health since it is closely correlated with the retention and use efficiency of water and nutrients in soil [1]. Soil with higher carbon content can hold more water and nutrients, thus leading to higher crop productivity. Furthermore, the knowledge of soil carbon empowers farmers to adopt sustainable agriculture practices that optimize resource efficiency, including water and fertilizer use, while simultaneously enhancing crop productivity and environmental protection [2].

Traditional methods for measuring soil carbon are expensive and time-consuming. The standard method is dry combustion [3, 4], which requires longer than one week of time and can only measure a small volume of soil. Moreover, it costs around US$20 per soil sample [5, 6] and therefore is not suitable for monitoring small soil carbon changes over large areas or over time. There are also in-situ methods such as laser-induced spectroscopy [7, 8] and inelastic neutron scattering [9]. However, these methods typically cost more than US$10k [3]. There have been plenty of efforts in developing lower-cost soil carbon sensing systems utilizing soil color and reflectance [10–16]. However, the trade-off for reduced cost is often compromised accuracy in these systems. Additionally, these systems often require soil sample

Table 1: Soil properties measured by recent RF-based sensing techniques. Scarf is the only work measures soil carbon.

Method	Soil property
GreenTag (RFID) [24]	Moisture
Backscatter [18]	Moisture
Smol (LoRa) [25]	Moisture
LoRa [19]	Moisture
CoMEt (USRP) [26]	Moisture
LTE-Soil-Meter [20]	Moisture
Strobe (Wi-Fi) [17]	Moisture & EC
Scarf (this work)	Carbon

Table 2: Low-cost soil carbon sensing techniques. Scarf achieves high accuracy without the need for sample dying.

Method	Accuracy (R^2)	Sample drying	Price (USD)
Chroma meters [10, 11]	0.53-0.79	Y	1000s
Digital camera [12]	0.88	Y	100s-1000s
Remote sensing [28, 29]	0.23-0.89	N	depends
Spectrometers [14, 16]	0.73-0.78	Y	1000s
Reflectometer [15]	0.57	Y	350
Scarf (this work)	0.91	N	10s

preparation through air drying and sieving, which hinders their ability to obtain rapid carbon measurements. To the best of our knowledge, no existing system can fulfill the combined requirements of accurate, inexpensive and rapid determination of soil carbon. According to the soil scientists we consulted, there is a significant demand for such systems.

In this paper, our goal is to develop a system that meets all the requirements mentioned above. We propose to utilize signals in RF and optical bands, i.e., Wi-Fi and images, which are widely available on edge devices like smartphones and drones, for soil carbon sensing. Our decision to employ RF signals is inspired by recent research [17–20] demonstrating that various RF signals, including Wi-Fi, RFID, LTE, etc., can be used to detect soil permittivity. In addition, soil studies have shown that soil carbon content influences soil permittivity [21, 22]. Collectively, these insights suggest a potential correlation between RF signals and soil carbon, with soil permittivity as an intermediate variable. However, a challenge here is that soil permittivity changes caused by soil carbon and soil moisture are entangled. That means, only measuring soil permittivity is inadequate to determine soil carbon content, necessitating additional information. To complement the RF data, we propose to utilize images, which are easily accessible on smartphones and have been shown to correlate with soil carbon content through color analysis [10, 11, 23]. The traditional color-based carbon sensing methods, however, rely on known soil moisture levels. They require separately measuring soil moisture or air drying the soil sample. Motivated by the aforementioned insights, we design and implement Scarf, a system for **S**oil **ca**rbon sensing using **RF** signals and images.

The major contributions of this work are as follows:

- We introduce Scarf, a novel soil carbon sensing technique that enables low-cost, rapid and flexible soil carbon detection with RF signals and images. This is the first work to enable soil carbon sensing with commodity wireless devices, whereas existing low-cost RF-based soil sensing techniques only focus on soil moisture (as shown in Table 1). As a proof-of-concept, we implement Scarf with commodity WARP hardware [27] and smartphone camera without modification, demonstrating the possibility to bring down the cost of soil carbon sensing to US$10s.
- We derive mathematical models to show that estimating soil carbon from RF signals and images is theoretically feasible because the impacts of soil carbon and soil moisture on RF signals and images are non-linearly correlated. To the best of our knowledge, this is the first work to demonstrate the possibility of using a combination of RF signals and images to sense soil carbon.
- Given the limitations of mathematical models in fully capturing the complex relationships among soil carbon, moisture, permittivity, and lightness, we incorporated a machine learning component. The resulting model can better handle the complexities inherent in soil systems by combining the strengths of both mathematical modeling and machine learning.
- We tested Scarf with two soil types. Our evaluation results show that Scarf's approach of combining mathematical computation with machine learning can help improve the accuracy of mathematical models, even with small-size datasets. For sand compost mixtures, it achieves a high correlation of 96.3% and coefficient of determination (R^2) of 0.911, which is comparable to the state-of-the-art soil carbon sensing techniques using devices that cost US$1000s [14, 16] (Table 2). For field soils, Scarf achieves slightly worse performance with a correlation of 88.0% and R^2 of 0.417, due to the relatively small dataset and the small range of carbon content.

2 Related Work

We discuss related work in the following three categories.

Low-cost soil carbon sensing. The efforts on low-cost soil carbon sensing can be divided into two categories. (i) Soil color-based methods leverage the relationship between soil color and soil carbon. Soil color can be determined visually with Munsell color charts [23] or more accurately with chroma meters [10, 11]. Recent studies demonstrate the possibility of using digital cameras [12] and cameras on mobile phones [13] to measure soil color. (ii) Reflectance-based methods rely on the relationship between reflectance spectra and soil organic carbon in the visible, near-infrared and shortwave infrared (400-2500 nm) regions [28, 30, 31]. To reduce the cost of soil carbon sensing, spectrometers can be deployed on satellites, aircraft, and unmanned aerial systems to provide large-scale and rapid soil carbon sensing. These remote sensing systems, however, achieve lower accuracy and suffer from weather conditions and soil conditions such as vegetation cover, soil moisture and soil roughness [28, 32]. Recent studies also look into portable devices using low-cost spectrometers [14–16], which have limited spectral ranges, for soil carbon determination. Compared to more capable instruments, these simplified devices can bring down the cost from ~US$50,000 to US$100s-1000s. The authors in [15] demonstrate a field portable reflectometer, which costs US$350, but only achieves an accuracy of 0.57.

As shown in Table 2, for all these approaches, except remote sensing, a key limitation is that soil samples require drying and sieving before conducting measurements, leading to extra time and labor effort. Although remote sensing does not need sample preparation, its performance is not stable. Scarf adopts two signal modalities to eliminate the need for sample drying while achieving good accuracy.

Low-cost RF-based soil sensing. Recently, several novel sensing techniques have been proposed to enable low-cost and accurate soil moisture sensing using RF signals. In contrast to traditional RF-based sensing techniques such as ground penetrating radar (GPR) [33] and Time Domain Reflectometery (TDR) [34], which requires expensive specialized hardware, the recent studies focus on low-cost commodity wireless devices that bring down the cost from US$1000s to under US$100. Strobe [17] proposes using Wi-Fi signals for soil moisture and electrical conductivity (EC) sensing. The authors in [18] use low-cost and low-energy backscatter to sense soil moisture leveraging ultra-wideband signals. GreenTag [24] leverages Differential Minimum Response Threshold (DMRT) of two commodity RFID tags to detect soil moisture of plant pots in a greenhouse. Recent work also uses LoRa signals for soil moisture sensing [19, 25]. The authors in [19] use the relative time-of-flight (ToF) between two receive antennas to sense soil moisture. Smol [25] only adopts received signal strength indicator (RSSI) information, which limits the estimation accuracy. CoMEt [26] is a non-invasive system with both the transmitter and receive antenna array above the soil surface. LTE-Soil-Meter [20] measures the relative ToF of two LTE receivers.

As shown in Table 1, most existing techniques only sense soil moisture. Scarf is the only work to sense soil carbon. As a proof-of-concept, this work chooses Wi-Fi signals to detect soil permittivity. We believe Scarf's mathematical models are also applicable to other RF signals which can detects soil permittivity [18–20, 26], e.g., LTE signals, after adapting the operating frequency in the equations.

Application of machine learning in RF sensing. In recent years, there have been rich applications of machine learning techniques in RF sensing for human activities [35–41], such as gesture recognition, fall detection, pose estimation, etc. These systems typically adopt convolutional neural network (CNN), more specifically, ResNet [42], to extract features from RF data. This is because CNN has demonstrated superior performance in human activity detection in images and videos while ResNet has its advantages of allowing deeper neural architectures, making it possible to detect more complex patterns. Earlier systems mostly rely on supervised learning architectures [36–38], which requires ground truth labels provided by other signal modalities such as RGB data. To reduce the laborious labeling efforts, several systems are developed to utilize partially labeled datasets [35, 39] and unsupervised learning architectures [40, 41]. Scarf draws inspirations from these systems but differs in the utilization of RGB data, which is combined with RF signals as the input to the machine learning model.

3 Background

We first introduce the background of soil carbon and then discuss soil carbon's impact on permittivity and soil color.

3.1 Soil carbon primer

Soil carbon includes both inorganic and organic carbon. Inorganic carbon exists in mineral forms, primarily as calcium carbonate, while organic carbon presents as *soil organic matter*—a complex mixture of decomposed plant and animal residues. In this paper, we focus on soil organic carbon given its greater responsiveness to agriculture practices [3]. Throughout the paper, we use soil carbon to refer to the organic portion of soil carbon.

The standard method of measuring soil carbon is dry combustion [3, 4]. It relies on laboratory analysis through taking small-volume soil samples and oxidizing them at a high temperature. These procedures are expensive and time-consuming, thus not suitable for monitoring small soil carbon changes in the field and creating soil carbon maps of large areas [29]. There have been several in-situ methods, including spectroscopic methods and remote sensing, to provide faster, cheaper, and more accurate carbon measurement. Spectroscopic methods leverage the spectral behavior of soil carbon, including near/mid-infrared spectroscopy (NIRS/MIRS), laser-induced breakdown spectroscopy (LIBS) and inelastic neutron scattering (INS). NIRS/MIRS detects carbon through the infrared reflectance in the near/mid infrared region that is affected by soil carbon [43]. LIBS uses laser beam to form microplasma which emits light containing the spectral signature of carbon [7, 8]. INS is based on the gamma rays emitted from the interaction of carbon nuclei and fast neutrons [9].

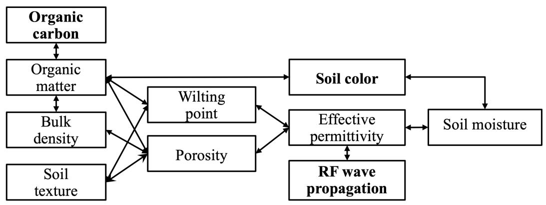

Figure 1: Relationship between soil carbon, soil physical properties, soil color and RF wave propagation.

The high cost of these methods (over US$10k [3]), however, limits their adoption.

3.2 Soil carbon, soil color, and RF signals

Figure 1 illustrates the overall connection among soil carbon, soil color, and RF wave propagation in soil, interlinked through a series of soil physical properties. Next, we introduce the relationships in detail.

3.2.1 **Relationship between soil carbon and soil color.** Soil organic carbon is one of the major pigments of soil color. There has been a long history of using soil color to determine soil carbon content. Traditionally, Munsell color charts [23] have been used to determine soil carbon content. Such a subjective method involves substantial errors. Recent studies [10, 11] use chroma meters to get more accurate soil color measurement. Statistically, there exists a negative relationship between soil color and soil carbon content. That is, the higher the carbon content, the darker the soil color. However, to ensure the accuracy of soil color measurement, the soil sample must be sieved, and its soil moisture needs to be controlled because soil moisture also changes soil color. Existing methods require either drying out or saturating the soil sample before performing the color measurement. Besides soil moisture, soil texture and iron oxides also influence soil color. Their impacts need to be calibrated when using soil color to determine carbon content.

3.2.2 **Relationship between soil carbon and RF wave propagation.** The propagation of RF signals in soil depends on the soil's dielectric permittivity: it slows down in soil because soil has a higher dielectric permittivity than air. Soil's dielectric permittivity, on the other hand, mostly depends on the amount of water in the soil. Therefore, various dielectric-based commodity soil sensors, including RF-based approaches such as GPR [33] and TDR [34], measure soil permittivity to estimate soil moisture.

Mapping permittivity to soil moisture. The mapping from permittivity to moisture requires modeling permittivity as a function of soil properties. A widely adopted modeling approach is using mixing models which are empirically derived as third-order functions of soil volumetric water content (VWC), e.g., Topp's equation [44]. The polynomial coefficients in the functions need to be adapted for different types of soils through extensive experimental data. These models are widely adopted by commodity dielectric-based soil moisture sensors to convert permittivity to VWC.

Another common modeling approach is using *soil dielectric mixing models*, which consider soil texture and therefore can be applied for different soil types. These models typically involve the impacts of soil texture, wilting point, porosity, VWC and radio frequency on permittivity [45, 46].

Soil dielectric mixing model. To help understand the model, here we first explain the related soil properties.

- *Dielectric permittivity* is a material property that describes a material's ability to store electrical energy in an electric field. Relative permittivity (unitless) refers to the ratio of absolute dielectric permittivity to the free-space permittivity. *Effective permittivity*, also known as apparent permittivity, refers to the relative permittivity of the soil mixture measured in-situ. For the rest of this paper, we use permittivity to refer to effective permittivity for simplicity.
- *Soil texture* is the method to classify soil into different *soil types*. It is expressed as the proportion of different-sized soil particles, i.e., sand, silt and clay, where sand is the largest and clay is the smallest.
- *Porosity* is the ratio of pore space in the total volume of soil. It indicates the amount of water/air soil can hold.
- *Bulk density* is the dry soil weight divided by its volume. It is inversely related to porosity.
- *Wilting point* is the soil water content below which plants cannot extract water from soil.
- *Transition moisture* marks the point at which the relationship between permittivity and VWC shifts from a gradual to a rapid increase. This phenomenon is attributed to the transformation of water from a bound to a free state within the soil. Bound water is tightly bound to soil particles and has a smaller dielectric permittivity than free water [45]. Existing literature has demonstrated a strong correlation between transition moisture and wilting point [45, 47]. Therefore, the two terms are usually used interchangeably.

Considering these soil properties, the effective permittivity of soil at different VWC levels can be described as a three-phase equation [48] that has been validated to generalize for different soil types and soil properties:

$$\epsilon_e = \begin{cases} (1-p)\epsilon_s + (p-w)\epsilon_a + w\epsilon_b & w \le w_{wp} \\ (1-p)\epsilon_s + (p-w)\epsilon_a & \\ \quad +w\left(\frac{p-w}{p-w_{wp}}\epsilon_b + \frac{w-w_{wp}}{p-w_{wp}}\epsilon_f\right) & w_{wp} < w \le p \\ (1-w)\epsilon_s + w\epsilon_f & w > p \end{cases} \tag{1}$$

where p is the porosity, w is the VWC, w_{wp} is the VWC at wilting point, ϵ_s, ϵ_a, ϵ_b and ϵ_f are the permittivity of soil, air, bound water and free water, respectively. ϵ_s can be computed from the volumetric ratios of sand, silt and clay, v_{sand}, v_{silt}

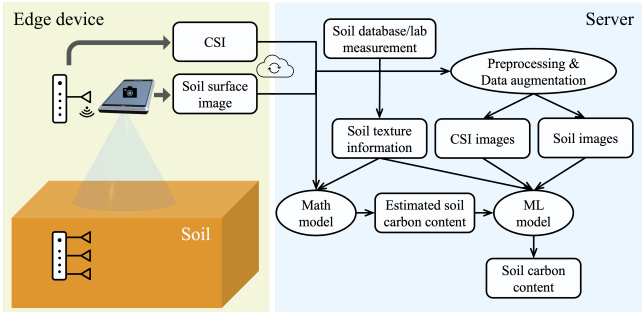

Figure 2: Design overview of Scarf. Two RF nodes collect CSI and a smartphone collects soil surface image. The data is sent to a server to determine carbon content with a method combining mathematical computation and machine learning.

and v_{clay}, and their permittivity, ϵ_{sand}, ϵ_{silt} and ϵ_{clay}, given as: $\epsilon_s = v_{sand}\epsilon_{sand} + v_{silt}\epsilon_{silt} + v_{clay}\epsilon_{clay}$.

Soil carbon's impact on permittivity. Soil carbon is closely correlated with porosity, an important variable in the mixing model (Eq. 1), and thus has a significant impact on permittivity. Specifically, soils richer in carbon have lower bulk density, higher porosity, higher wilting point and can hold more water. These combined factors result in a lower soil permittivity and, consequently, a faster propagation speed of RF signals within the soil.

Soil carbon's impact on permittivity affects the accuracy of dielectric-based soil moisture sensors. Traditional soil mixing models that map permittivity to VWC are mostly developed for mineral soils with low carbon contents. Using them for carbon-rich soils could introduce errors in the estimated VWC. To calibrate the impact of soil carbon, some earlier studies suggest changing the polynomial coefficients in the empirical mixing models [44, 49]. Recent work using dielectric mixing models considers the impact of soil carbon either implicitly by using different bulk densities for soils with different carbon contents [21], or explicitly by including soil carbon in the dielectric mixing model [22].

4 Design

In this section, we discuss the design of Scarf. As shown in Figure 2, we use two RF nodes, one in the air as the transmitter and another in the soil as the receiver to collect channel state information (CSI) that correlates with soil properties. Meanwhile, a smartphone camera takes pictures of the soil surface to capture soil's optical information. The collected CSI and soil surface images are sent to an edge or cloud server for further processing. We employ a hybrid approach combining mathematical modeling and machine learning (ML) to estimate soil carbon content. Initially, a mathematical model leverages soil images and CSI to generate a preliminary carbon estimation. Recognizing the limitations of mathematical models in fully capturing the complex relationships among soil properties, we introduce an ML model to predict the error between the initial estimate and ground truth. The predicted error is then added back to the mathematical result to produce the final soil carbon estimation. Before training the ML model, we perform necessary preprocessing on both CSI and soil surface image. Due to the limited size of measurement data, we also apply data augmentation to increase dataset size. The ML model is trained on data containing a diverse range of soil moisture and carbon content levels for each soil type. Both the mathematical model and ML model require soil texture information, which can be obtained from existing soil database [50], or laboratory measurement. Scarf's edge to server communication can benefit from existing infrastructure for data-driven agriculture [51] to achieve reliable and secure network connectivity.

4.1 Sensing soil carbon with RF signals and soil surface images

We first explain and model the relationships between RF signals and soil carbon, and between soil images and soil carbon, followed by discussing why a single signal modality does not work. Then we use mathematical models to show that two signal modalities are enough to determine soil carbon.

4.1.1 **RF signals vs. soil carbon.** Our idea of using RF signals to detect soil carbon levels is inspired by two key insights. First, existing work on soil dielectric mixing models considers soil carbon's impact on permittivity, with a goal to calibrate out the impact and improve the accuracy of soil moisture estimation. This indicates that, conversely, by leveraging the relationship between soil carbon and permittivity, we can also infer soil carbon from permittivity. Second, recent work [17–20] has demonstrated that RF signals from low-cost devices, such as Wi-Fi chips, can measure soil permittivity, enabled by the phenomenon that RF signals travel slower in soil because it has a higher permittivity than air.

Modeling permittivity as a function of soil carbon and moisture. We start with the three-phase equation (Eq. 1), where the parameters can be divided into three groups. (i) Parameters independent of soil carbon and soil moisture include the permittivity of soil, air, bound water and free water, ϵ_s, ϵ_a, ϵ_b, ϵ_f. These parameters can be considered as constants during our measurements. ϵ_s depends solely on soil texture/type and is a constant given a soil type. ϵ_a is usually set to 1. ϵ_b and ϵ_f are functions of operating frequency and soil temperature. We apply equations in [22] to get ϵ_b and ϵ_f. (ii) Parameters dependent on soil carbon are wilting point w_{wp} and porosity p. (iii) Soil volumetric water content (VWC), w. For simplicity, we can rewrite Eq. 1 as:

$$\epsilon_e = f_\epsilon(w, w_{wp}, p) \qquad (2)$$

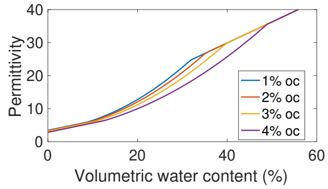

Figure 3: Simulation based on dielectric mixing model for soils with 40% clay, 40% slit and 20% sand. Effective permittivity (unitless) decreases as carbon level increases.

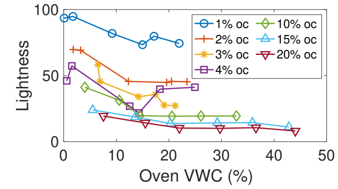

Figure 4: Lightness (unitless) of soil surface images. Lightness decreases as VWC and carbon content increase.

Existing work models w_{wp} and p empirically. We adopt a linear model of wilting point [52], given as $w_{wp} = 0.0298 + 0.089v_{clay} + 0.0136oc$, where v_{clay} is the volumetric ratio of clay in soil and oc is the organic carbon content (%). The equation's parameters are determined using 12 soil types and organic carbon contents. We use empirical models of porosity p and bulk density BD given in [22], which have been evaluated with over 30 sites containing wide varieties of soil types and carbon contents. p is modeled as a non-linear function of oc, BD, and volumetric ratios of clay and slit in soil, v_{clay} and v_{slit}, written as $p = f_p(oc, BD, v_{clay}, v_{slit})$. BD is negatively correlated with oc: $BD = -0.067oc + 1.2301$. Given a soil type with known v_{clay} and v_{slit}, both w_{wp} and p are only functions of oc, written as $w_{wp} = f_{wp}(oc)$ and $p = f_p(oc)$. Hence, the permittivity in Eq. 2 is only a function of w and oc, given as:

$$\epsilon_e = f_\epsilon(w, f_{wp}(oc), f_p(oc)) = f_\epsilon(w, oc) \tag{3}$$

To quantify the impact of soil carbon on effective permittivity, we first perform simulation based on Eq. 3. Figure 3 plots the simulated permittivity at 2.4 GHz Wi-Fi frequency band for soils with 40% clay, 40% slit and 20% sand, a composition used in our experiments. The results indicate that given the same ground truth VWC, the permittivity decreases for soils with higher carbon contents. This decrease is significant enough to be observed when VWC falls in the range between wilting point and saturation point, e.g., 20-40% VWC. We have also experimentally validated this behavior, and the results are discussed later in Section 6.1.2.

4.1.2 **Soil surface images vs. soil carbon.** Existing studies [11, 29] have shown that there is a negative relationship between soil carbon and soil lightness, typically modeled as a linear equation: $L = -ax + b$, where L is the lightness (unitless) in CIELAB color space, x is the organic carbon content oc or natural logarithm of oc, $\ln(oc)$, and $a, b > 0$ are constants. However, existing studies use chroma meters with controlled light source and carefully prepared soil samples which are fine-grained and have controlled VWC.

To demonstrate the possibility of using smartphone images to detect soil lightness change caused by soil carbon, we collect soil surface images of soil boxes at different carbon and moisture levels. These soil boxes are created with sand and compost manure for fine-grained control of soil carbon content. Figure 4 plots the lightness computed from the soil surface images after calibrating ISO, exposure time, and aperture size of the smartphone camera. It indicates a negative correlation between soil lightness and carbon content, consistent with previous studies. Notably, the speed of lightness decrease slows down at higher carbon content. Additionally, lightness also decreases as VWC increases. The impact of soil moisture on soil lightness has also been identified in existing literature [53–55], while not explicitly modeled.

Modeling lightness as a function of soil carbon and moisture. Based on the observations from Figure 4, we derive the model of lightness as a function of oc and w:

$$L = -a\ln(oc + 1) + b - cw \tag{4}$$

where $a, b, c > 0$ are constants. Here we adopt the logarithm of oc because the decrease speed of lightness reduces as oc increases. We choose $\ln(oc + 1)$ instead of $\ln(oc)$ to avoid large negative values of $\ln(oc)$ when oc is close to 0.

We determine a, b and c empirically. Given a set of measured oc, w, and L values, i.e., $oc_1, oc_2, \cdots, oc_n, w_1, w_2, \cdots, w_n$, and $L_1, L_2, \cdots, L_n$, we can compute a, b and c by solving the following equation:

$$\underbrace{\begin{bmatrix} -\ln(oc_1+1) & 1 & -w_1 \\ -\ln(oc_2+1) & 1 & -w_2 \\ \vdots & \vdots & \vdots \\ -\ln(oc_n+1) & 1 & -w_n \end{bmatrix}}_{A} \underbrace{\begin{bmatrix} a \\ b \\ c \end{bmatrix}}_{x} = \underbrace{\begin{bmatrix} L_1 \\ L_2 \\ \vdots \\ L_n \end{bmatrix}}_{B} \tag{5}$$

We can get $x = (A^TA)^{-1}A^TB$.

4.1.3 **A single signal modality is not enough.** Figure 3 indicates that only knowing permittivity is not enough to determine soil carbon content, because a permittivity value can be mapped to different carbon values given different VWC values. We need both permittivity and ground-truth VWC to determine the carbon content. Similarly, as shown in Figure 4, measuring soil lightness without knowing VWC is not also enough to determine carbon content, since a single lightness value can be mapped to different carbon values given different VWC values. The challenge is that measuring the VWC is very time-consuming. The ground truth oven drying method takes 24 hours per sample. To achieve rapid determination of soil carbon, we propose to combine RF signals with soil surface images.

4.1.4 **Combining the two signal modalities to determine soil carbon.** We have identified that both permittivity and soil lightness are functions of soil carbon and soil moisture. A question here is: are the two signal modalities enough to estimate soil carbon? This is equal to a mathematical problem: given ϵ_e and L obtained from RF signals and soil surface images, can we solve a system consists of Eq. 3 and Eq. 4, where oc and w are the only two unknown variables?

We first show that in both equations, there are monotonic relationships between oc and w. The monotonic relationship in Eq. 4 is obvious: by fixing L as a constant, $w \uparrow \Rightarrow oc \downarrow$. For Eq. 3, we notice that its variables depending on soil carbon, i.e., p and w_{wp}, both increase monotonically over oc, as shown in Figure 5, based on our simulation for both field soils and sand compost mixtures. With $\epsilon_f > \epsilon_b > \epsilon_s > \epsilon_a$ as a known knowledge, we can derive the relationship between oc and w given a fixed ϵ_e by analyzing the three phases in Eq. 1. (i) Phase 1: We can rewrite the equation as $w\epsilon_b + (\epsilon_a - \epsilon_s)p + C = 0$, where C is a constant. Since $(\epsilon_a - \epsilon_s) < 0$, $oc \uparrow \Rightarrow p \uparrow \Rightarrow w \uparrow$. (ii) Phase 2: We can rewrite the equation as $w[x(\epsilon_b - \epsilon_f) + \epsilon_f - 1] + (\epsilon_a - \epsilon_s)p + C = 0$, where $x = (p - w)/(p - w_{wp})$ and $(\epsilon_b - \epsilon_f) < 0$. We have $oc \uparrow \Rightarrow p \uparrow, w_{wp} \uparrow \Rightarrow x \uparrow \Rightarrow w \uparrow$. (iii) Phase 3: Here ϵ_e only depends on w and increasing oc does not change w. Based on the three-phase analysis, we can see that as oc increases, w will first increase and then stay the same after $w > p$.

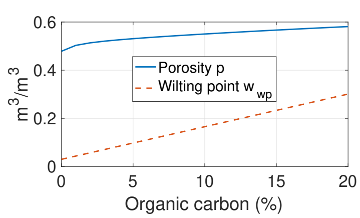

Figure 5: Simulation based on empirical models of porosity and wilting point for soils containing 100% sand. Both parameters monotonically increase over soil carbon content.

Given the monotonic relationships between oc and w in Eq. 3 and Eq. 4 and a pair of measured L and ϵ_e, there exists at most one pair of oc and w that satisfies both equations. Figure 6 plots an example of how to solve this problem. Given a pair of L and ϵ_e, the two equations can be plotted as two non-parallel curves in the figure. The two curves have an intersection that corresponds to the solution of oc and w.

To automate the search of the intersection, we formulate an optimization problem. We combine Eq. 3 and Eq. 4 through substitution to get an equation with a single unknown variable: $\epsilon_e = f_\epsilon([-aLn(oc+1)+b-L]/c, oc)$. The goal is to find

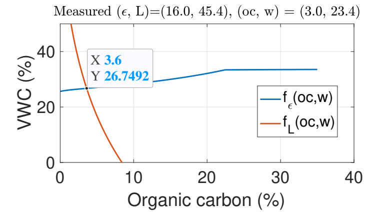

Figure 6: Example of soil organic carbon content oc and VWC w computation based on mathematical models. Given a pair of measured permittivity ϵ and soil lightness L, oc and w can be determined from the intersection of the two functions. The estimated oc and w are 3.6 and 26.7, which align with the ground truth oc and w of 3.0 and 23.4.

an oc that minimizes the following objective function:

$$f_{obj} = \left|\bar{\epsilon}_e - f_\epsilon([-aLn(oc+1) + b - \bar{L}]/c, oc)\right| \quad (6)$$

where $\bar{\epsilon}_e$ and $\bar{L}$ are the measured effective permittivity and soil lightness. After obtaining oc, the corresponding w can be determined from Eq. 4.

4.2 Data collection and calibration

Here we introduce how we leverage Wi-Fi signals to collect CSI, and the necessary calibration for soil surface images.

4.2.1 **CSI collection.** Our goal is to capture CSI that contains permittivity information of soil, and use it to generate the input to the ML model. We adopt Strobe's approach that uses a single-antenna transmitter and a multi-antenna array to get soil-dependent CSI [17]. Besides Strobe's horizontal placement of antennas (Figure 7(a)), we also support deploying the antennas vertically (Figure 7(b)).

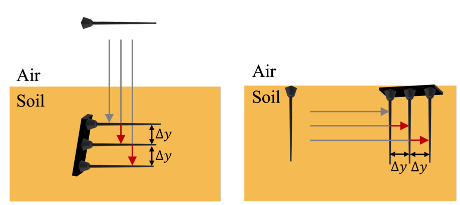

(a) Horizontal (b) Vertical

Figure 7: Antenna deployment for CSI collection.

Practical use cases. The two antenna deployment methods correspond to two use cases that do not introduce significant deployment effort. (*i*) The horizontal deployment can be used for long-term carbon monitoring with the underground RF node remaining buried, which only requires a one-time effort to dig up the soil and bury the antenna array. This is helpful to monitor long-term carbon changes, e.g., carbon loss after tillage, and carbon increase with carbon management practices like no tillage and straw mulch coverage. (*ii*) The vertical deployment makes Scarf portable for field measurements at different locations. We can plug the antennas into soil in a similar way as commodity soil sensors, without the need to digging up a large volumn of soil.

CSI vs. permittivity. In both setups, the relative time-of-flight (ToF) of a signal propagating to two adjacent antennas can be simplified to $\Delta t = n\Delta y/c$, where Δy is the distance between antennas, c is the speed of light, and n is the refractive index. n can be related to the effective permittivity ϵ_e as $n = \sqrt{\epsilon_e}$, so we have $\Delta t = \Delta y\sqrt{\epsilon_e}/c$. This relative ToF corresponds to a phase rotation of $-2\pi f \Delta t$, where f is the carrier frequency. In a multipath environment, CSI is the sum of multiple paths, where only the shortest path contains the phase rotation of interest. We first perform pre-processing steps including noise reduction and ToF sanitization [56], and then apply a multipath resolving technique, MUSIC [57], to extract the shortest path and estimate ϵ_e.

4.2.2 **Image calibration.** The lightness of image depends on scene luminance and camera settings. Prior work [58] demonstrates that a digital camera can measure luminance after calibrating camera settings including ISO, exposure time and aperture area. A pixel's digital number correlates with the scene luminance and camera settings as follows:

$$N \propto tSL_s/f^2 \tag{7}$$

where t is the exposure time, S is the ISO, L_s is the scene luminance, and f is the aperture number. The settings of t, S and f are accessible from the metadata of images taken by smartphones. We choose reference settings of t, S and f, e.g., 1/120, 100 and 1.8, and calibrate every image to the reference leveraging Eq. 7. Since we conduct experiments under the same scene luminance, we do not explicitly calibrate L_s. When there is a change in scene luminance, we can calibrate L_s by taking picture of a reference object, e.g., a white paper. In addition to lighting conditions, a more comprehensive approach should also consider factors like camera makers and models. Recent research [59] has demonstrated the potential of deep learning-based image normalization for calibrating these factors. We leave the investigation of advanced image calibration techniques for future work.

4.2.3 **Environmental variations.** We consider four types of variations. (*i*) Antenna misalignment. In real-world conditions, it is hard to perfectly align the transmitter and receiver antennas. To reduce the impact of misalignment, for each soil sample, we collect multiple CSI samples by moving or rotating the transmitter, and use them for the ML model training and testing. (*ii*) Soil surface disruptions. These impacts are reduced by falttening the soil surface and removing objects on it before conducting measurements. (*iii*) Small-scale spatial variations. Scarf measures the average VWC over a path length of around 10cm in soil, which smooths out small-area variations in VWC as well as the impact of non-soil objects in soil [17, 19]. Similarly, we average soil

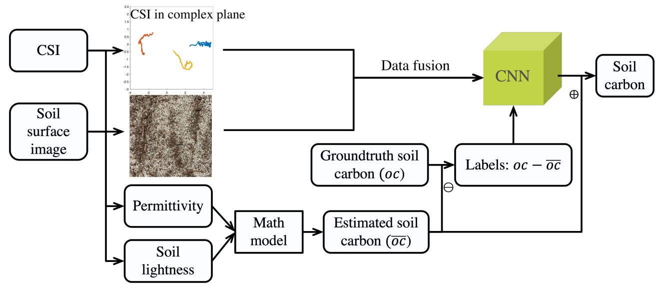

Figure 8: ML model overview. We first use the math model to get an initial soil carbon estimation, and then use the ML model to correct the error between the ground truth and the math-computed output.

surface images accross a region. (*iv*) VWC Variations across different locations and times. They are taken care of by our mathematical models, which utilize CSI and image measured at a location and time to estimate VWC while simultaneously decoupling its influence on carbon estimation.

4.3 Applying ML to improve accuracy

The mathematical models discussed in Section 4.1 capture the major relationships between soil carbon, moisture, permittivity and lightness. However, they may have missed some underlying relationships which introduce deviations between mathematical results and the ground truth. To handle the hidden relationships, we propose to apply ML.

Figure 8 shows an overview of the ML model design for improving math-computed soil carbon. With a set of CSIs and soil images, we first use them to compute soil permittivity and soil lightness. The results are fed into the mathematical model (Eq. 6) to perform an initial estimation of soil carbon content, $\overline{oc}$. We then generate the labels for the ML model by subtracting $\overline{oc}$ from the ground truth oc obtained with standard laboratory measurement. For the input to the ML model, we consider an early fusion approach to combine the two signal modalities before they enter the feature extraction network. It is noteworthy that there may exist a better architecture to handle the multi-modal signals, we leave the model architecture improvement for future work. For feature extraction, we adopt one of the most popular convolutional neural networks (CNNs), ResNet [42]. The feature extraction network takes the fused CSI and image data and labels as input to predict the error between the math-computed soil carbon content and the ground truth. In the end, the predicted error is added back to the mathematical result to produce the final soil carbon estimation.

4.3.1 **Generating input to ML model.** We perform pre-processing and data augmentation for CSI and images.

CSI. The goal here is to generate input that retains information as much as possible and can be interpreted by the

ML model. A CSI sample is a matrix of complex numbers, with a size of 3×330 in our experiments. We convert it to a CSI image by plotting the CSI in the complex plane to keep both phase and amplitude information. An alternative CSI representation is the MUSIC spectrum presented as a relative ToF-absolute ToF heatmap. It is an intermediate result of the signal processing algorithms in prior work [17, 56]. Our experimental results indicate that its performance is similar to the CSI image.

Soil surface images. We use a smartphone to take images of soil surface for each carbon level and moisture level. The original images have a size of 4032×3024. In order to reduce computation overhead and in the meantime capture enough information, e.g., color and texture, we crop each image to a size of 448×448 and then resize it with a factor of 0.5 to create a 224×224 RGB image. We choose size 224×224 here because it is a commonly adopted input image size for CNNs such as ResNet [42].

Data augmentation. To reduce overfitting, we apply data augmentation to both CSI and images to generate multiple images for a soil surface. Data augmentation is a widely adopted technique in computer vision to expand dataset size and reduce overfitting. For CSI, we applied two methods for data augmentation. First, we interpolate two measured CSI samples to produce a new sample. Second, we add additive white Gaussian noise (AWGN) and random relative phase shift among antennas, which emulates the case where soil has variations that lead to relative phase variations. For images, we first randomly rotate an image and then perform cropping from a random region. Common approaches for data augmentation in computer vision also include brightness and color adjustments. We do not adopt them since these are useful information correlated with soil carbon contents.

5 Implementation

Hardware. We implement Scarf's CSI collection component with WARP boards [27]. We connect the transmitter antenna to one board and the receiver antenna array to another board though cables. For both deployments in Figure 7, the WARP boards are not buried. Practically, the horizontal deployment requires the antenna array to remain buried. We expect to replace its connected WARP board with a Wi-Fi chipset that can be buried together with the array in the future. We sweep the radio frequency across all available 2.4 GHz channels to collect CSI of the entire available 70 MHz bandwidth at 2.4 GHz Wi-Fi spectrum. We perform the necessary calibration steps to remove phase offsets and distortions caused by hardware impairments, same as those described in [17].

Software. We implement the mathematical models, CSI and image pre-processing, and data augmentation in MATLAB. To support data fusion of two signal modalities, we implement a customized ResNet regression model with Pytorch [60], a widely used deep learning library. Since we have a relatively small dataset, we use SGD optimizer, a small batch size of 16, and 14 ResNet layers. We use mean squared error (MSE) as the loss function, which is effective to improve R^2 during training. All ResNet training and testing runs on an NVIDIA GeForce RTX 4070 GPU.

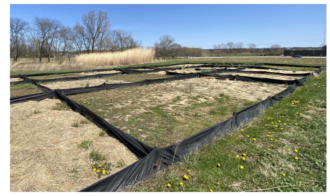

Figure 9: Long-term experimental farm plots maintained at different carbon contents.

(a) Soils from the field with 1-4% carbon contents.

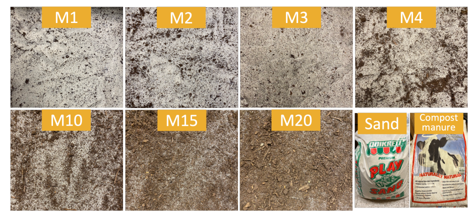

(b) Sand compost mixtures, consisting of sand and compost manure, at 1-4%, 10%, 15% and 20% carbon contents.

Figure 10: Two soil types used for experiments.

Experimental setups. To test real soils, we use soils maintained in the field at different carbon contents (Figure 9) to create four soil boxes with 1-4% carbon contents, as shown in Figure 10(a). We label them as F1-F4. These soils consist of 40% clay, 40% silt and 20% sand. Since it is hard to precisely control carbon contents in real soils, we also create sand compost mixtures by mixing sand and compost manure. By controlling the percentage of sand and compost manure, we create boxes at 1-4%, 10%, 15% and 20% carbon contents, as shown in Figure 10(b). We label these mixtures as M1-M20.

6 Evaluation

We first perform laboratory analysis of soil properties for the field soils and sand compost mixtures used in our experiments to get ground truth knowledge of soil carbon's impact on soil properties. We then evaluate the permittivity measured by Scarf compared to commodity soil sensors to validate that Scarf can detect soil carbon's impact on permittivity. Finally, we evaluate the performance of our mathematical model and ML model. Since the results for horizontal and

Table 3: Laboratory results of soil carbon and bulk density for field soils (F1-F4), sand, compost manure, and their mixtures (M1-M4, M10, M15, M20).

Soil type	Carbon (%)	Bulk density (Mg/m^3)
F1	1.35	1.038
F2	2.30	1.020
F3	3.15	1.016
F4	3.88	0.983
Sand	0	1.458
Compost manure	47.66	0.178
M1	1.54	1.043
M2	3.03	0.966
M3	4.25	0.893
M4	4.90	0.889
M10	14.14	0.792
M15	18.97	0.718
M20	31.58	0.601

vertical antenna deployments are similar, we mainly report results for the horizontal deployment (Figure 7(a)).

Laboratory analysis of soil properties. We characterize some important soil properties, which are used as ground truths to demonstrate that the soil and sand compost mixture boxes we created have different carbon contents, leading to different bulk densities and water retention curves. We first explain the methods we use to measure these properties. For each of the measurements, we take 3 soil samples and compute the average to get more accurate results.

- *VWC.* We first measure gravimetric water content (GWC) with oven drying method, calculated as (weight of wet soil - weight of dry soil) / (weight of dry soil), and then multiply it by bulk density of soil to get VWC. For each soil sample, we dry it in an oven at 105 °C for 24 hours.
- *Soil organic carbon.* We use the standard dry combustion method [4] to measure it. We take 10-15 mg of 250-μm sieved soil samples in tin capsules and analyze them using a Flash 2000 NC soil analyzer.
- *Bulk density.* We use the standard core method [61]. We sample soil in a cylindrical core and then measure the soil sample's weight and VWC. Bulk density is calculated as (weight of dry soil / the volume of the core).
- *Water retention.* We measure VWC at -33 to -1500 kPa pressures with Pressure Plate Extractors [62]. A pressure in the range of 10-33 kPa is used to determine the soil's water holding capability against gravity, while a pressure of -1500 kPa is used to determine the wilting point.

Commodity soil sensors. To verify the drop of effective permittivity over soil carbon, we compare Scarf against 2 commodity soil sensors, i.e., Meter TEROS 10 and Decagon GS3. Meter TEROS 10 measures VWC and raw reading in mV, which can be converted to effective permittivity using the equation in its manual [63]. Decagon GS3 measures effective permittivity, EC and temperature.

6.1 Microbenchmarks

6.1.1 Laboratory soil analysis results.

We first look at the ground truth soil properties.

Soil organic carbon and bulk density. We analyze the soil organic carbon and bulk density for field soils, pure sand, pure compost manure, and the mixtures of sand and compost manure. The results are shown in Table 3. We create the sand compost mixtures based on the carbon content of pure compost manure and by controlling the relative weight of sand and compost manure. As we can see, the measured carbon contents of field soils are close to the expected values, while the carbon contents of sand compost mixture boxes are slightly higher than the expected values. A possible reason is that the estimated carbon content for pure compost manure is lower than its actual carbon content. This could happen since we take small samples for carbon analysis and these samples may be biased. We use these measured values for the rest of the evaluation. In addition, we observe a negative relationship between bulk density and carbon content, which is consistent with the discussion in Section 4.1.1.

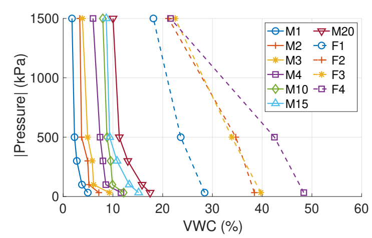

Figure 11: Laboratory results of water retention curves for sand compost mixtures (M1-M4, M10, M15, M20) (solid lines) and field soils (F1-F4) (dashed lines).

Water retention curves. Figure 11 plots the water retention curves. We observe two trends that meet our expectation. First, field soils have higher VWC than sand compost mixtures. This is because the field soils contain 40% clay, which helps retain more water. Second, given a pressure level, for both soil types, VWC increases over carbon content. Moreover, the increase in wilting point (i.e., -1500 kPa) over carbon content is consistent with our observation in Figure 5.

6.1.2 Soil carbon's impact on RF signals.

To verify RF signals can detect permittivity changes over soil carbon content, we conduct experiments with soils containing different carbon and moisture contents. We measure the top layer of soil (0-10cm) where soil carbon is concentrated in practice. We estimate permittivity from collected CSIs with MUSIC-based data processing algorithm. For each soil box, we vary the VWC by adding tap water and mixing water with soil evenly. For each moisture level, we measure permittivity with Scarf, Meter TEROS 10 and Decagon GS3. We use the VWC measured by oven drying method as the ground truth.

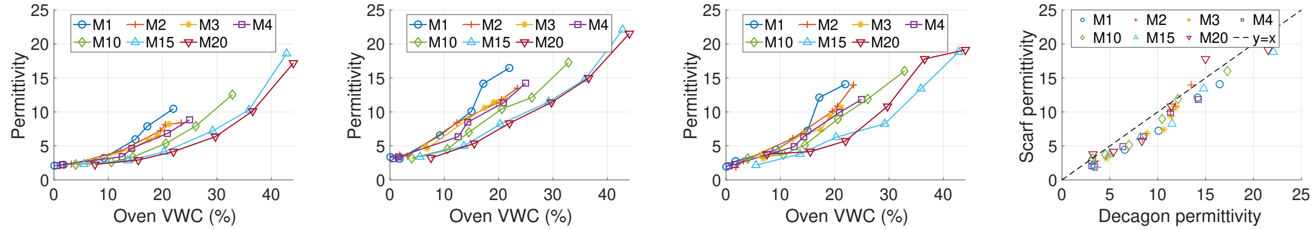

(a) Meter TEROS 10 (b) Decagon GS3 (c) Scarf (d) Scarf vs. Decagon

Figure 12: Sand compost mixtures (1-20% carbon): permittivities measured by different devices show the same trends. Scarf shows more variations than commodity soil sensors.

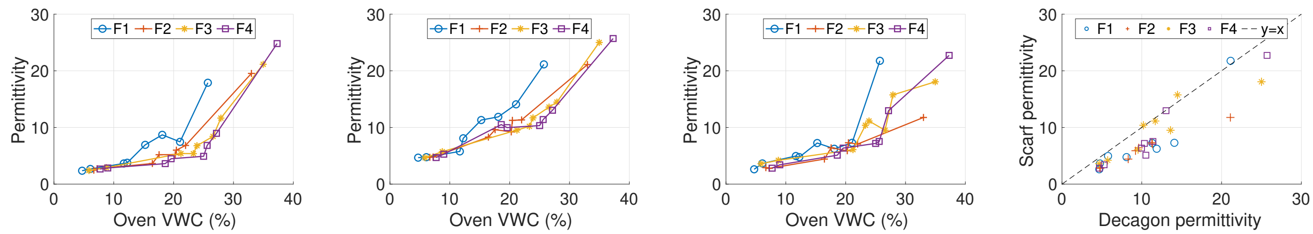

(a) Meter TEROS 10 (b) Decagon GS3 (c) Scarf (d) Scarf vs. Decagon

Figure 13: Field soils (1-4% carbon): Scarf's results deviate more from the soil sensors than the sand compost mixture case.

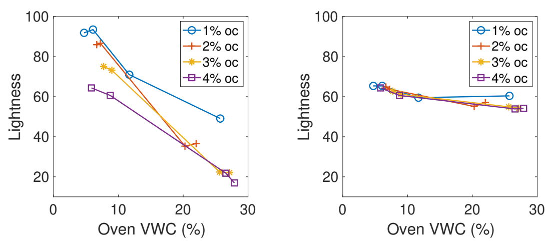

(a) Calibrated (b) Raw data

Figure 14: Lightness of field soils. Calibrated images show that soil lightness decreases over VWC and carbon content.

Sand compost mixtures. Figure 12 plots the permittivity of sand compost mixtures measured by different devices. For all three devices, the general trends are the same: higher carbon content results in lower permittivity under the same ground truth VWC. We notice that Scarf has slightly higher variations. There are several possible reasons, e.g., multipath may not be fully removed during data processing, and we might have applied different amounts of force on the soil surface during antenna deployment. Figure 12(d) shows permittivity results obtained from Scarf exhibit a strong correlation with those of acquired from the Decagon sensor. Similarly, Scarf's results also demonstrate a high correlation with the Meter sensor. The correlation is 0.97 for Scarf and the Decagon sensor, and 0.95 for Scarf and the Meter sensor.

Field soils. Figure 13 plots the permittivity of field soils measured by different devices. We notice that Meter and Decagon can detect the permittivity decrease for F1-F2. However, the curves of F2-F4 overlap more. This might be caused by the close carbon contents between F2-F4, as shown in Table 3. Similar to the case of sand compost mixtures, we also observe that Scarf's results have more variations than the Meter and Decagon sensors. Figure 13(d) shows the correlation of permittivity results obtained from Scarf and the Decagon sensor. Compared to sand compost mixtures, the correlation here is slightly worse, which drops to 0.91.

6.1.3 *Soil carbon's impact on soil lightness.*

For sand compost mixtures, we have discussed the trends of soil lightness's decrease over soil carbon and moisture in Section 4.1.2 (Figure 4). For field soils, the lightness results of smartphone images after calibrating camera settings are shown in Figure 14(a). The general trends are the same as those of sand compost mixtures. However, the decrease in lightness over soil carbon content is smaller for field soils, suggesting that parameters in Eq. 4 need adjustment for different soil types. By comparing Figure 14(a) and Figure 14(b), we can also see the importance of image calibration, without which the lightness results of different soil carbon contents are overlapped and do not decrease much over VWC.

6.2 Soil carbon sensing performance

Next, we evaluate the soil carbon sensing performance of the mathematical model proposed in Section 4.1.4 and the performance of the ML model described in Section 4.3.

Performance metrics. We use correlation coefficient, coefficient of determination, and mean squared error, which are commonly used metrics, for evaluating model fitting performance. Correlation coefficient is defined as

$$r = \frac{\Sigma_{i=1}^{n}(x_i - \bar{x})(y_i - \bar{y})}{\sqrt{\Sigma_{i=1}^{n}(x_i - \bar{x})^2}\sqrt{\Sigma_{i=1}^{n}(y_i - \bar{y})^2}} \tag{8}$$

where n is the size of the testing dataset, $X = \{x_1, x_2, ..., x_n\}$ is the set of predicted carbon labels and $Y = \{y_1, y_2, ..., y_n\}$ is the set of ground truth carbon labels, $\bar{x}$ and $\bar{y}$ are the mean values of X and Y. The range of r is $[-1, 1]$. Coefficient of determination is defined as $R^2 = 1 - \Sigma_{i=1}^{n}(y_i - x_i)^2 / \Sigma_{i=1}^{n}(y_i - \bar{y})^2$ The range of R^2 is $(-\infty, 1]$. For both r and R^2, a value closer to 1 represents a better performance. The mean squared error is given as $MSE = \Sigma_{i=1}^{n}(y_i - x_i)^2/n$.

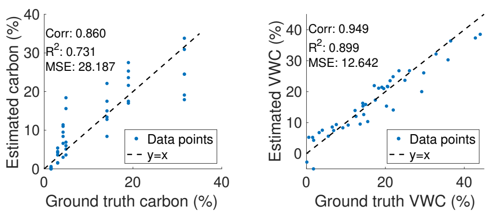

(a) Carbon content (b) VWC

Figure 15: Sand compost mixtures: carbon content and VWC computed by mathematical model.

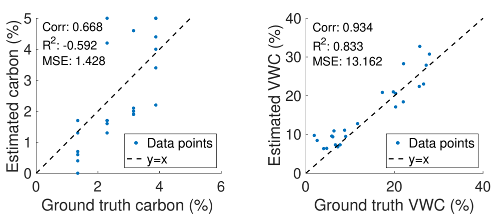

(a) Carbon content (b) VWC

Figure 16: Field soils: carbon content and VWC computed by mathematical model.

6.2.1 ***Mathematical model.*** We collect CSI and soil surface images of 7 sand compost mixture boxes each with 6 moisture levels, and 4 field soil boxes each with 6 moisture levels. At each moisture level, we collect CSIs at 3-6 transmitter locations by moving or rotating the transmitter, and average the estimated permittivity. We then get 42 data points for sand compost mixtures and 24 data points for field soils. We first use lightness estimated from soil surface images to find parameters for Eq. 4. Then we use Eq. 6 to compute soil carbon content and VWC. It is worth noting that we use oven-based VWC w to estimate the constants in Eq. 4. Our experimental results suggest that w can be replaced by VWC estimated from RF signals without sacrificing performance, simplifying the process of obtaining the lightness model.

Figure 15 and Figure 16 present the results computed by the mathematical model for the two soil types. Both soils have superior performance in VWC estimation. Sand compost mixtures have better correlation and R^2 of carbon estimation than the field soils because they have a larger dataset and a larger range of carbon contents. With only 24 data points tested for field soils, a single outlier can significantly degrade the performance of correlation and R^2. The MSE of field soils, however, is much smaller than that of sand compost mixtures, meaning that the carbon estimation errors of field soils are reasonably small. Overall, we can conclude that the mathematical model is a good fit for our experimental data, while some relationships leading to the carbon estimation errors may not be fully captured.

6.2.2 ***ML model.*** **Datasets.** We experimentally collect 213 samples for the sand compost mixtures and 110 samples for the field soils. We perform data augmentation on these samples as described in Section 4.3.1. After data augmentation, we obtain 672 samples for the sand compost mixtures and 384 samples for the field soils. To avoid model overfitting, we split training and testing datasets to ensure that the moisture level and carbon content combination of all the testing samples have not been seen from the training dataset. We train and test sand compost mixtures and field soils separately.

Table 4: Performance of soil carbon determination.

Soil type	Model	r	R^2	MSE
Sand	Math	0.896±0.044	0.784±0.105	20.788±14.297
	ML	0.947±0.039	0.842±0.148	14.116±12.584
	Math&ML	0.963±0.027	0.911±0.070	8.491±7.997
Field soil	Math	0.863±0.078	0.195±0.398	0.772±0.357
	ML	0.431±0.341	0.179±0.265	0.736±0.238
	Math&ML	0.880±0.063	0.417±0.269	0.523±0.242

Performance of leaving some moisture levels out. We first test how the ML model performs when some moisture levels are not seen during training. For sand compost mixtures, there are 42 different moisture levels of all boxes, from which we randomly pick samples of 11 moisture levels to create the testing dataset. For field soils, we pick 4 out of 24 moisture levels as the testing dataset. We also exclude these samples from the parameter calculation in Eq. 5, so they are unseen in the mathematical model. The results are averaged over 5 random samplings of soil moisture levels. As shown in Table 4, for both soil types, our proposed method of combining mathematical model with ML can significant improve the performance of only using a single model. We observe that during the training process, the Math&ML model can effectively reduce the training loss of predicting the error between math-computed carbon and ground truth. The correlation and R^2 results of field soils appear to be worse than sand compost mixtures because the field soils have a smaller range of carbon content. Interestingly, the performance of solely using the ML model is the worst for field soils, possibly due to the limited dataset size. In contrast, the Math&ML

model demonstrates superior performance with the same dataset, emphasizing the value of integrating domain-specific knowledge, i.e., the mathematical model, into ML training.

Horizontal vs. vertical antenna deployment. The results in Table 2 are based on the horizontal deployment (Figure 7(a)). We have also collected data for the vertical deployment (Figure 7(b)). Following the same data processing procedures, the average r, R^2, and MSE of the vertical deployment are 0.967, 0.923, and 7.177, respectively, for sand compost mixtures. The slightly better performance of the vertical deployment could be because the environmental noises are less when the antennas are all plugged into soil.

7 Discussion

Making Scarf more practical. Scarf is a proof-of-concept design and implementation that necessitates invasive antenna deployment to sense soil carbon, limiting its practical applications. Transitioning it to a non-invasive system is essential. However, a significant gap exists between the cost-effectiveness and non-invasiveness of the RF-based techniques given in Table 1. While it is feasible to develop a non-invasive carbon sensing system by integrating a non-invasive RF system like CoMEt [26] into Scarf, the high cost of USRP hardware still hinders its adoption. In contrast, low-cost methods often compromise on non-invasive operation. Therefore, developing a low-cost, non-invasive system remains a priority for future research.

Path towards smartphone sensing. Our end goal is to sense soil carbon with smartphones. There exist two major challenges. (*i*) CSI collection on smartphones. CSI is generally unavailable in modern Wi-Fi chips. Earlier CSI extraction tools [64, 65] are limited to outdated chipsets. Nexmon [66, 67] supports more Wi-Fi devices, including smartphones, but still requires firmware modification. A recent work, BeamSense [68], enables CSI extraction using beamforming reports and supports various 802.11-complient Wi-Fi chips without firmware modification. The feasibility of employing Nexmon and BeamSense for soil carbon sensing will be explored in our future work. (*ii*) Image calibration. The quality of soil surface images is affected by the distance and rotation of the smartphone. Our future work will look into designing a system capable of automatically calibrating the positions utilizing a smartphone's internal sensors, e.g., gyroscope and LIDAR. To account for the impact of lighting conditions and camera models on measured soil lightness, we will investigate advanced image calibration techniques, e.g., the deep learning-based approach adopted in [59].

Evaluation for different soil types. We acknowledge that more experimental data is required for a comprehensive evaluation of our models. Especially, we need to adjust some parameters in our models for different soil types. Moreover, Scarf only considers farms soils without non-carbon color pigments, and high levels of heavy metal and salt contamination. These factors affect soil lightness, permittivity and EC accordingly, and can be handled by updating the mathematical models. To address the issue of limited dataset size and difficulty of real-world data collection, we are actively investigating transfer learning methods to benefit from existing datasets. Transfer Learning is advantageous for small datasets due to its ability to leverage knowledge from a larger dataset to improve the performance of a model trained on a smaller target dataset [69]. E.g., we can adapt the ML model trained on one soil type to another soil type. We have also tested that our mathematical models are not sensitive to small soil composition variations (<20%), indicating that we only need to train models for coarse-grained soil types.

Improving feature extraction. In this work, we have only tested two CSI representations, i.e., CSI image and MUSIC spectrum. It is possible that other forms of representations may outperform the performance we achieve. Additionally, the feature extraction network we adopt has a lot of potential to improve. We leave these improvements for future work.

8 Conclusion

This paper presents Scarf, a novel soil carbon sensing technique that leverages widely available RF signals and images, eliminating the requirement for specialized hardware. To disentangle the complex relationships between soil carbon, soil permittivity, soil moisture, and soil color, we derive mathematical models to compute carbon content from soil permittivity and lightness measured by RF signals and images. We combine machine learning with the mathematical models to further improve performance. We have tested Scarf with field soils and sand compost mixtures at various soil carbon contents and moisture levels. Our results show that Scarf can achieve high accuracy in predicting carbon contents with the combined mathematical and machine learning model. We believe Scarf is a significant step towards a low-cost, rapid and accurate soil carbon sensor that can enable farmers and researchers to monitor soil carbon content and identify site-specific practices of sustainable agriculture.

Acknowledgments

We are grateful to our shepherd and the anonymous reviewers for their constructive feedback. This work was supported by ARO Grant W911NF-23-1-0088, NSF-AoF FAIN Grant 2132573 and Microsoft. We thank Umesh Acharya and Nancy Loria for their assistance in collecting soil property data.

References

[1] Rattan Lal. Soil health and carbon management. *Food and Energy Security*, 5(4):212–222, 2016.

[2] Rattan Lal. Soils and sustainable agriculture. a review. *Agronomy for Sustainable Development*, 28:57–64, 2008.

[3] Amitava Chatterjee, Rattan Lal, L Wielopolski, Madhavi Z Martin, and MH Ebinger. Evaluation of different soil carbon determination methods. *Critical Reviews in Plant Science*, 28(3):164–178, 2009.

[4] Darrell W Nelson and Lee E Sommers. Total carbon, organic carbon, and organic matter. *Methods of soil analysis: Part 3 Chemical methods*, 5:961–1010, 1996.

[5] The Service Testing and Research Laboratory at Ohio State University. Sample analysis fee schedule. https://bpb-us-w2.wpmucdn.com/u.osu.edu/dist/4/39220/files/2022/07/STAR-lab-analysis-cost_FY-23.pdf, Sep 2022.

[6] SWPT Laboratory at Colorado State University. Feed and forage analysis price list. https://agsci.colostate.edu/soiltestinglab/price-list/, May 2023.

[7] David A Cremers, Michael H Ebinger, David D Breshears, Pat J Unkefer, Susan A Kammerdiener, Monty J Ferris, Kathryn M Catlett, and Joel R Brown. Measuring total soil carbon with laser-induced breakdown spectroscopy (libs). *Journal of Environmental Quality*, 30(6):2202–2206, 2001.

[8] Michael H Ebinger, David A Cremers, Clifton M Meyer, Ronny D Harris, et al. Laser-induced breakdown spectroscopy and applications for soil carbon measurement. *Carbon sequestration in soils of Latin America. Food Products Press, New York*, pages 407–422, 2006.

[9] Lucian Wielopolski, George Hendrey, Kurt H Johnsen, Sudeep Mitra, Stephen A Prior, Hugo H Rogers, and H Allen Torbert. Nondestructive system for analyzing carbon in the soil. *Soil Science Society of America Journal*, 72(5):1269–1277, 2008.

[10] Skye A Wills, C Lee Burras, and Jonathan A Sandor. Prediction of soil organic carbon content using field and laboratory measurements of soil color. *Soil Science Society of America Journal*, 71(2):380–388, 2007.

[11] Naoki Moritsuka, Kaori Matsuoka, Keisuke Katsura, Shuji Sano, and Junta Yanai. Soil color analysis for statistically estimating total carbon, total nitrogen and active iron contents in japanese agricultural soils. *Soil science and plant nutrition*, 60(4):475–485, 2014.

[12] RA Viscarra Rossel, Youssef Fouad, and Christian Walter. Using a digital camera to measure soil organic carbon and iron contents. *Biosystems engineering*, 100(2):149–159, 2008.

[13] Luis Gómez-Robledo, Nuria López-Ruiz, Manuel Melgosa, Alberto J Palma, Luis Fermín Capitán-Vallvey, and Manuel Sánchez-Marañón. Using the mobile phone as munsell soil-colour sensor: An experiment under controlled illumination conditions. *Computers and electronics in agriculture*, 99:200–208, 2013.

[14] Yijia Tang, Edward Jones, and Budiman Minasny. Evaluating low-cost portable near infrared sensors for rapid analysis of soils from south eastern australia. *Geoderma Regional*, 20:e00240, 2020.

[15] Patrick M Ewing, Dan TerAvest, Xinyi Tu, and Sieglinde S Snapp. Accessible, affordable, fine-scale estimates of soil carbon for sustainable management in sub-saharan africa. *Soil Science Society of America Journal*, 85(5):1814–1826, 2021.

[16] Amin Sharififar, Kanika Singh, Edward Jones, Frisa Irawan Ginting, and Budiman Minasny. Evaluating a low-cost portable NIR spectrometer for the prediction of soil organic and total carbon using different calibration models. *Soil Use and Management*, 35(4):607–616, 2019.

[17] Jian Ding and Ranveer Chandra. Towards low cost soil sensing using Wi-Fi. In *The 25th Annual International Conference on Mobile Computing and Networking (MobiCom)*, pages 1–16. ACM, 2019.

[18] Colleen Josephson, Manikanta Kotaru, Keith Winstein, Sachin Katti, and Ranveer Chandra. Low-cost in-ground soil moisture sensing with radar backscatter tags. In *ACM SIGCAS Conference on Computing and Sustainable Societies*, pages 299–311, 2021.

[19] Zhaoxin Chang, Fusang Zhang, Jie Xiong, Junqi Ma, Beihong Jin, and Daqing Zhang. Sensor-free soil moisture sensing using LoRa signals. *Proceedings of the ACM on Interactive, Mobile, Wearable and Ubiquitous Technologies*, 6(2):1–27, 2022.

[20] Yuda Feng, Yaxiong Xie, Deepak Ganesan, and Jie Xiong. LTE-Based low-cost and low-power soil moisture sensing. In *Proceedings of the 20th ACM Conference on Embedded Networked Sensor Systems (SenSys)*, pages 421–434, 2022.

[21] Valery Mironov and Igor Savin. A temperature-dependent multi-relaxation spectroscopic dielectric model for thawed and frozen organic soil at 0.05–15 ghz. *Physics and Chemistry of the Earth, Parts A/B/C*, 83:57–64, 2015.

[22] Chang-Hwan Park, Carsten Montzka, Thomas Jagdhuber, François Jonard, Gabrielle De Lannoy, Jinkyu Hong, Thomas J Jackson, and Volker Wulfmeyer. A dielectric mixing model accounting for soil organic matter. *Vadose Zone Journal*, 18(1):190036, 2019.

[23] Albert Henry Munsell. *A Color Notation: A Measured Color System Based on the Three Qualities, Hue, Values and Chroma with Illustrative Models, Charts and a Course of Study Arranged for Teachers*. Geo. H. Ellis, 1907.

[24] Ju Wang, Liqiong Chang, Shourya Aggarwal, Omid Abari, and Srinivasan Keshav. Soil moisture sensing with commodity RFID systems. In *Proceedings of the 18th International Conference on Mobile Systems, Applications, and Services (MobiSys)*, pages 273–285, 2020.

[25] Daniel Kiv, Garvita Allabadi, Berkay Kaplan, and Robin Kravets. smol: Sensing soil moisture using LoRa. In *Proceedings of the 1st ACM Workshop on No Power and Low Power Internet-of-Things*, pages 21–27, 2022.

[26] Usman Mahmood Khan and Muhammad Shahzad. Estimating soil moisture using RF signals. In *Proceedings of the 28th Annual International Conference on Mobile Computing and Networking (MobiCom)*, pages 242–254, 2022.

[27] Rice University. Warp project. http://warpproject.org.

[28] Theodora Angelopoulou, Nikolaos Tziolas, Athanasios Balafoutis, George Zalidis, and Dionysis Bochtis. Remote sensing techniques for soil organic carbon estimation: A review. *Remote Sensing*, 11(6):676, 2019.

[29] Umesh Acharya, Rattan Lal, and Ranveer Chandra. Data driven approach on in-situ soil carbon measurement. *Carbon Management*, 13(1):401–419, 2022.

[30] Sidney Allen Bowers. *Reflection of radiant energy from soils*. Kansas State University, 1971.

[31] Eyal Ben-Dor, Y Inbar, and Y Chen. The reflectance spectra of organic matter in the visible near-infrared and short wave infrared region (400–2500 nm) during a controlled decomposition process. *Remote sensing of Environment*, 61(1):1–15, 1997.

[32] Marco Nocita, Antoine Stevens, Carole Noon, and Bas van Wesemael. Prediction of soil organic carbon for different levels of soil moisture using vis-nir spectroscopy. *Geoderma*, 199:37–42, 2013.

[33] Johan Alexander Huisman, Susan Sharpess Hubbard, J David Redman, and A Peter Annan. Measuring soil water content with ground penetrating radar: A review. *Vadose zone journal*, 2(4):476–491, 2003.

[34] Kosuke Noborio. Measurement of soil water content and electrical conductivity by time domain reflectometry: a review. *Computers and electronics in agriculture*, 31(3):213–237, 2001.

[35] Wenjun Jiang, Chenglin Miao, Fenglong Ma, Shuochao Yao, Yaqing Wang, Ye Yuan, Hongfei Xue, Chen Song, Xin Ma, Dimitrios Koutsonikolas, et al. Towards environment independent device free human activity recognition. In *Proceedings of the 24th annual international conference on mobile computing and networking (MobiCom)*, pages 289–304, 2018.

[36] Yonglong Tian, Guang-He Lee, Hao He, Chen-Yu Hsu, and Dina Katabi. RF-based fall monitoring using convolutional neural networks. *Proceedings of the ACM on Interactive, Mobile, Wearable and Ubiquitous Technologies*, 2(3):1–24, 2018.

[37] Mingmin Zhao, Yonglong Tian, Hang Zhao, Mohammad Abu Alsheikh, Tianhong Li, Rumen Hristov, Zachary Kabelac, Dina Katabi, and Antonio Torralba. RF-based 3D skeletons. In *Proceedings of the 2018 Conference of the ACM Special Interest Group on Data Communication (SIGCOMM)*, pages 267–281, 2018.

[38] Mingmin Zhao, Tianhong Li, Mohammad Abu Alsheikh, Yonglong Tian, Hang Zhao, Antonio Torralba, and Dina Katabi. Through-wall human pose estimation using radio signals. In *Proceedings of the IEEE Conference on Computer Vision and Pattern Recognition (CVPR)*, pages 7356–7365, 2018.

[39] Shuya Ding, Zhe Chen, Tianyue Zheng, and Jun Luo. RF-net: A unified meta-learning framework for RF-enabled one-shot human activity recognition. In *Proceedings of the 18th Conference on Embedded Networked Sensor Systems*, pages 517–530, 2020.

[40] Tianhong Li, Lijie Fan, Yuan Yuan, and Dina Katabi. Unsupervised learning for human sensing using radio signals. In *Proceedings of the IEEE/CVF Winter Conference on Applications of Computer Vision*, pages 3288–3297, 2022.

[41] Ruiyuan Song, Dongheng Zhang, Zhi Wu, Cong Yu, Chunyang Xie, Shuai Yang, Yang Hu, and Yan Chen. RF-URL: unsupervised representation learning for RF sensing. In *Proceedings of the 28th Annual International Conference on Mobile Computing And Networking (MobiCom)*, pages 282–295, 2022.

[42] Kaiming He, Xiangyu Zhang, Shaoqing Ren, and Jian Sun. Deep residual learning for image recognition. In *Proceedings of the IEEE conference on computer vision and pattern recognition (CVPR)*, pages 770–778, 2016.

[43] GW McCarty, JB Reeves, VB Reeves, RF Follett, and JM Kimble. Mid-infrared and near-infrared diffuse reflectance spectroscopy for soil carbon measurement. *Soil Science Society of America Journal*, 66(2):640–646, 2002.

[44] G Clarke Topp, JL Davis, and Aa P Annan. Electromagnetic determination of soil water content: Measurements in coaxial transmission lines. *Water resources research*, 16(3):574–582, 1980.

[45] James R Wang and Thomas J Schmugge. An empirical model for the complex dielectric permittivity of soils as a function of water content. *IEEE Transactions on Geoscience and Remote Sensing*, (4):288–295, 1980.

[46] Myron C Dobson, Fawwaz T Ulaby, Martti T Hallikainen, and Mohamed A El-Rayes. Microwave dielectric behavior of wet soil-part ii: Dielectric mixing models. *IEEE Transactions on geoscience and remote sensing*, (1):35–46, 1985.

[47] Richard Wayne Newton. *Microwave remote sensing and its application to soil moisture detection.* Texas A&M University, 1977.

[48] Chang-Hwan Park, Andreas Behrendt, Ellsworth LeDrew, and Volker Wulfmeyer. New approach for calculating the effective dielectric constant of the moist soil for microwaves. *Remote Sensing*, 9(7):732, 2017.

[49] CH Roth, MA Malicki, and R Plagge. Empirical evaluation of the relationship between soil dielectric constant and volumetric water content as the basis for calibrating soil moisture measurements by tdr. *Journal of Soil Science*, 43(1):1–13, 1992.

[50] Soil Survey Staff. "web soil survey." natural resources conservation service, us department of agriculture. 2014.

[51] Deepak Vasisht, Zerina Kapetanovic, Jongho Won, Xinxin Jin, Ranveer Chandra, Sudipta Sinha, Ashish Kapoor, Madhusudhan Sudarshan, and Sean Stratman. {FarmBeats}: an {IoT} platform for {Data-Driven} agriculture. In *14th USENIX Symposium on Networked Systems Design and Implementation (NSDI)*, pages 515–529, 2017.

[52] Jun Liu, Shaojie Zhao, Lingmei Jiang, Linna Chai, and Fengmin Wu. The influence of organic matter on soil dielectric constant at microwave frequencies (0.5–40 ghz). In *2013 IEEE International Geoscience and Remote Sensing Symposium-IGARSS*, pages 13–16. IEEE, 2013.

[53] SK Bhadra and M Bhavanarayana. Estimation of the influence of soil moisture on soil colour. *Zeitschrift für Pflanzenernährung und Bodenkunde*, 160(3):401–405, 1997.

[54] EA Paul, JA Shields, WK Head, RJ St Arnaud, et al. Spectrophotometric measurement of soil color and its relationship to moisture and organic matter.

[55] DF Post, A Fimbres, AD Matthias, EE Sano, L Accioly, AK Batchily, and LG Ferreira. Predicting soil albedo from soil color and spectral reflectance data. *Soil Science Society of America Journal*, 64(3):1027–1034, 2000.

[56] Manikanta Kotaru, Kiran Joshi, Dinesh Bharadia, and Sachin Katti. SpotFi: Decimeter level localization using wifi. In *Proceedings of the 2015 ACM Conference on Special Interest Group on Data Communication (SIGCOMM)*, pages 269–282, 2015.

[57] Ralph Schmidt. Multiple emitter location and signal parameter estimation. *IEEE transactions on antennas and propagation*, 34(3):276–280, 1986.

[58] Peter D Hiscocks and P Eng. Measuring luminance with a digital camera. *Syscomp electronic design limited*, 2, 2011.

[59] Neha Sharma, Muhammad Shahzaib Waseem, Shahrzad Mirzaei, and Mohamed Hefeeda. MobiSpectral: Hyperspectral imaging on mobile devices. In *Proceedings of the 29th Annual International Conference on Mobile Computing and Networking (MobiCom)*, pages 1–15, 2023.

[60] Adam Paszke, Sam Gross, Francisco Massa, Adam Lerer, James Bradbury, Gregory Chanan, Trevor Killeen, Zeming Lin, Natalia Gimelshein, Luca Antiga, et al. Pytorch: An imperative style, high-performance deep learning library. *Advances in neural information processing systems*, 32, 2019.

[61] RB Grossman and TG Reinsch. 2.1 bulk density and linear extensibility. *Methods of soil analysis: Part 4 physical methods*, 5:201–228, 2002.

[62] Arnold Klute. Water retention: laboratory methods. *Methods of soil analysis: part 1 physical and mineralogical methods*, 5:635–662, 1986.

[63] METER Group. TEROS 10 user manual. 2021.

[64] Daniel Halperin, Wenjun Hu, Anmol Sheth, and David Wetherall. Tool release: Gathering 802.11 n traces with channel state information. *ACM SIGCOMM computer communication review*, 41(1):53–53, 2011.

[65] Yaxiong Xie, Zhenjiang Li, and Mo Li. Precise power delay profiling with commodity WiFi. In *Proceedings of the 21st Annual international conference on Mobile Computing and Networking (MobiCom)*, pages 53–64, 2015.

[66] Matthias Schulz, Daniel Wegemer, and Matthias Hollick. Nexmon: The c-based firmware patching framework. https://nexmon.org, 2017.

[67] Francesco Gringoli, Matthias Schulz, Jakob Link, and Matthias Hollick. Free your CSI: A channel state information extraction platform for modern Wi-Fi chipsets. In *Proceedings of the 13th International Workshop on Wireless Network Testbeds, Experimental Evaluation & Characterization (WiNTECH)*, page 21–28, 2019.

[68] Enze Yi, Dan Wu, Jie Xiong, Fusang Zhang, Kai Niu, Wenwei Li, and Daqing Zhang. {BFMSense}:{WiFi} sensing using beamforming feedback matrix. In *21st USENIX Symposium on Networked Systems Design and Implementation (NSDI)*, pages 1697–1712, 2024.

[69] Lisa Torrey and Jude Shavlik. Transfer learning. In *Handbook of research on machine learning applications and trends: algorithms, methods, and techniques*, pages 242–264. IGI global, 2010.